MINIATURE ROBUST HIGH-BANDWIDTH FORCE SENSOR WITH MECHANICALLY AMPLIFIED PIEZORESISTIVE READOUT

Dennis Alveringh[1,2], Diana L. van der Ven[1], Henk-Willem Veltkamp[1], Kevin M. Batenburg[1], Remco G. P. Sanders[1], David Fernandez Rivas[1], and Remco J. Wiegerink[1]

[1] MESA+ Institute, University of Twente, Enschede, THE NETHERLANDS and

[2] Salland Engineering B.V., Zwolle, THE NETHERLANDS

ABSTRACT

For fast and accurate force measurements, e.g., sampling the impact of a liquid droplet, a highly sensitive high-bandwidth force sensor is required. High-sensitivity and high-bandwidth are contradictive specifications in recently published force sensors. The miniature force sensor proposed in this paper uses a novel combination of in-plane sensing, mechanical amplification, and piezoresistive readout that overcomes this contradiction. The straightforward fabrication process consists of three photomasks and uses a single SOI wafer. The sensor has a proven range of 13 mN, a sensitivity of 1.46 N^{-1} and a bandwidth of 75 kHz. This is the first force sensor in this force range with such a large bandwidth and has the potential to open up a new field of force sensing where high sampling rates and low ranges are crucial.

KEYWORDS

Force sensor, load cell, microdroplet, needle-free injector, liquid jets, mechanical amplification.

INTRODUCTION

Understanding the microscale and microsecond impact behavior of liquids is crucial for various applications. Microdroplet impact plays a large role in, e.g., rain erosion of wind turbine blades, and within the inkjet printing field [1, 2]. Furthermore, the use of liquid jet injections as alternative to needles is widely explored. A large variety of needle-free injectors exists, some of them are already commercialized while others are still in development [3]. To understand and model the injection behavior accurate impact-force measurements are required. The impact of larger volume devices can be measured using commercial load cells, due to longer impact times and higher associated impact forces [4, 5]. Consequently, these devices typically result in deep (subcutaneous or intramuscular) injections and often cause pain and bruising. To prevent this, other devices use low volume jets and aim at superficial skin layers (epidermis or dermis) [6, 7]. Furthermore, dermal or epidermal injections have therapeutic benefits. For example, vaccine and insulin delivery within the epidermis and dermis, respectively, is reported to be more efficient compared to traditional delivery. [8, 9].

Recent studies from one of these systems rely on low volume microjets (20 nL, 50 µm diameter), with estimated forces of 0.5 mN to 5 mN (depending on jetting velocity, typically 20 m s^{-1} to 70 m s^{-1}) resulting in impact times between 100 µs to 300 µs [7, 10].

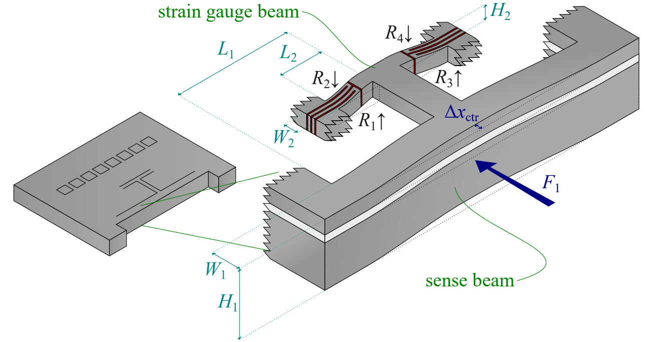

Figure 1: Illustration of the operation principle of the force sensor. A force applied on the clamped-clamped sense beam causes a mechanically amplified increase of strain in the strain gauge beam.

This class of microjets falls either below the sensitivity or temporal resolution of commercial devices, and thus impact forces can only be estimated using high speed recordings. Consequently, the actual force distribution over time cannot be characterized. Published micromachined load cells show high resolutions (nN [11] to µN [12, 13]), but limited bandwidth (<10 kHz). This paper describes a force sensing structure with piezoresistive readout and mechanical amplification that bridges this gap in measurement range.

THEORY AND DESIGN

The sensor consists of two clamped-clamped beams that are rigidly connected in the center as illustrated in Figure 1. The force is applied in-plane to the center of the sense beam. This force causes a displacement, which is transferred to the strain gauge beam. This beam consists of piezoresistive strain gauges in a Wheatstone bridge configuration. The strain in the strain gauge beam is higher compared to the strain in the sense beam as it is shorter. However, the latter beam does not significantly influence the stiffness or frequency behavior due to its lower width and height.

The second moment of area I_i for the bending of both beams is equal to [14]:

$$I_i = \frac{H_i W_i^3}{12}, \quad (1)$$

with $i = 1$ for the sense beam and $i = 2$ for the strain gauge beam, H_i the height of the beam, and W_i the width of the beam. The displacement in the center Δx_{ctr} due to deformation caused by a force F_i in the center of a clamped-clamped beam can be derived using Euler-Bernoulli beam

theory [14]:

$$\Delta x_{\mathrm{ctr}} = \frac{F_i L_i^3}{192 E I_i} = \frac{F_i L_i^3}{16 E H_i W_i^3}, \tag{2}$$

with L_i the length of the beam and E Young's modulus of silicon in [110] direction. Note that x_{ctr} is equal for both beams as these are rigidly connected in the center. The stiffness k_i can be approximated using Hooke's law by:

$$k_i = \frac{F_i}{\Delta x_{\mathrm{ctr}}} = \frac{16 E H_i W_i^3}{L_i^3}, \tag{3}$$

The stiffness should be dominated by the sense beam, i.e., when $k_1 \gg k_2 \rightarrow k \approx k_1$. This gives the following relation for the dimensions of the beam:

$$\frac{H_1 W_1^3}{L_1^3} \gg \frac{H_2 W_2^3}{L_2^3}. \tag{4}$$

The maximum strain $\varepsilon_{\mathrm{max},i}$ for clamped-clamped beams with an applied force in the center is:

$$\varepsilon_{\mathrm{max},i} = \frac{\sigma_{\mathrm{max},i}}{E} = \frac{F_i L_i W_i/2}{8 E I_i} = \frac{3 F_i L_i}{4 E W_i^2 H_i}, \tag{5}$$

with $\sigma_{\mathrm{max},i}$ the maximum stress. Substitution of (2) into (5) gives:

$$\varepsilon_{\mathrm{max},i} = \frac{12 W_i \Delta x_{\mathrm{ctr}}}{L_i^2}, \tag{6}$$

which forms a straight-forward approximation for the stress in the strain gauges $\varepsilon_{\mathrm{max},2}$. The mechanical amplification can be derived from the maximum strain in the sense beam $\varepsilon_{\mathrm{max},1}$ and the maximum strain in the strain gauge beam $\varepsilon_{\mathrm{max},2}$:

$$\frac{\varepsilon_{\mathrm{max},2}}{\varepsilon_{\mathrm{max},1}} = \frac{W_2 L_1^2}{W_1 L_2^2} \approx 5.6. \tag{7}$$

The bridge voltage of the Wheatstone bridge V_{b} is directly related to the relative change in resistance and is proportional to the maximum strain $\varepsilon_{\mathrm{max},2}$:

$$\frac{V_{\mathrm{b}}}{V_{\mathrm{s}}} = \left(\frac{R_2}{R_1 + R_2} - \frac{R_3}{R_3 + R_4}\right) = \frac{\Delta R}{R} = G \varepsilon_{\mathrm{max},2}, \tag{8}$$

with R_j the resistors as indicated in Figure 1, ΔR the change in resistance due to the strain, R the resistance in rest, and G the gauge factor. The latter is dependent on the doping level and crystal orientation, but lies in the order of 10 to 100 [15].

A measure for the bandwidth of the sensor can be found by the resonance frequency f_0 of the first mode, which can be estimated by [16]:

$$f_0 = 6.48 \frac{W_1}{2\pi L_1^2} \sqrt{\frac{E}{\rho}}, \tag{9}$$

with ρ the density of silicon.

The dimensions of the sensor components and material properties are given in Table 1. Filling in the numbers in (3), (8), and (9) gives a spring constant of $1.80 \cdot 10^4\,\mathrm{N\,m^{-1}}$, a sensitivity of $1.39\,\mathrm{N^{-1}}$ and a resonance frequency of 110 kHz.

Simulations based on finite element method (FEM) were conducted using COMSOL Multiphysics® 5.6. The model consisted of both beams and transmission. It was based on the layer stack as described in the next section consisting of silicon dioxide (SiO_2) and crystalline silicon (anisotropic elasticity). The results correspond well to the analytical model with a spring constant of $1.87 \cdot 10^4\,\mathrm{N\,m^{-1}}$, a sensitivity of $1.34\,\mathrm{N^{-1}}$, and a resonance frequency of 103 kHz.

Table 1: Dimensions of the sensor design as indicated in Figure 1 and material properties.

Length	L_1	2 mm	L_2	0.6 mm
Width	W_1	50 µm	W_2	25 µm
Height	H_1	427 µm	H_2	25 µm
Young's modulus	E	169 GPa		
Density of silicon	ρ	$2330\,\mathrm{kg\,m^{-3}}$		
Gauge factor	G	30		

FABRICATION

The fabrication is based on [17] with an additional step to realize piezoresistive strain gauges in the device layer. The device is fabricated in an SOI wafer with a highly p-type (boron) doped silicon handle layer of 400 µm, buried oxide layer of 2 µm, and a highly p-type doped silicon device layer of 25 µm (Figure 2a). The sense beam is realized in all three layers. The transmission and strain gauge beam are realized in the device layer only.

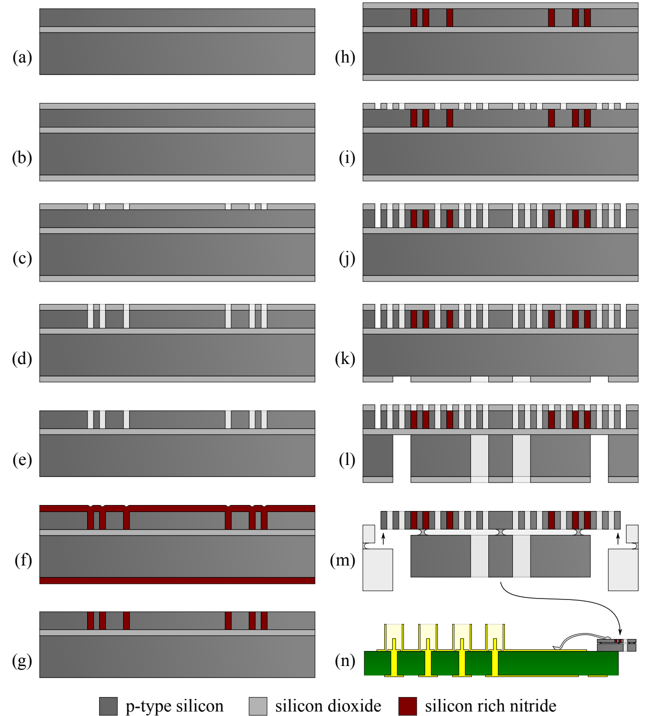

Figure 2: Illustrations of the fabrication steps. The device has been fabricated by three high aspect ratio plasma etches, conformal silicon rich silicon nitride deposition, and one isotropic release etch.

A SiO_2 layer of 1 µm is deposited by wet thermal oxidation (Figure 2b). Directional reactive ion etching (RIE) is used to form the isolation mask in the SiO_2 at the device layer side (Figure 2c). Then, high-aspect ratio (3 µm wide, 25 µm deep) trenches with a slightly positive taper are

realized using deep reactive ion etching (DRIE, Figure 2d). The hard mask is stripped using directional RIE on both sides of the wafer (Figure 2e). The trenches are filled with low-stress silicon rich silicon nitride (SiRN) using low-pressure chemical vapor deposition (LPCVD, Figure 2f). The SiRN on the surface is stripped using a directional RIE on both sides of the wafer (Figure 2g). As hard mask for the rest of the structures, a layer of 1 µm SiO_2 is deposited using LPCVD and annealed (Figure 2h). Directional RIE is used to form the mask in the SiO_2 layer on the device layer (Figure 2i). Then DRIE is used to form the structures in the device layer (Figure 2j). Similar RIE and DRIE steps are performed on the handle layer to form the hard mask and structures in the handle layer (Figures 2k and 2l). The structures are released using an isotropic vapour-phase hydrogen fluoride (HF) etch (Figure 2m). This etch also released the dies from the wafer.

All photolithography steps have been performed with positive photoresist. Resist stripping has been performed by oxygen plasma. The chips are assembled using adhesive bonding on a printed circuit board (PCB) and wirebonded with aluminum wire (Figure 2n).

A scanning electron microscopy (SEM) image and a photograph of the sensor are shown in Figures 3 and 4 respectively.

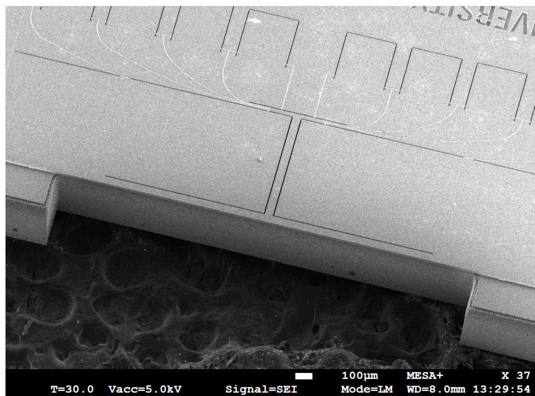

Figure 3: Scanning electron microscopy image of the device.

CHARACTERIZATION

The static performance of the sensor has been measured by applying a force range in increasing and decreasing order using a piezo actuator. The setup is illustrated in Figure 5. A lock-in amplifier (Stanford Research Systems® SR860) is used to apply the supply voltage (100 mV amplitude) and to

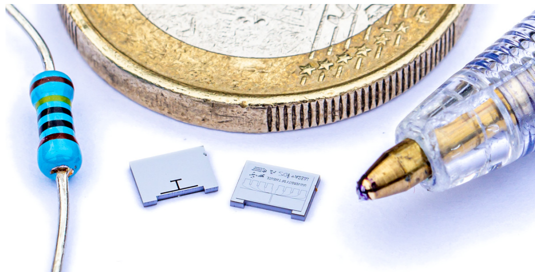

Figure 4: Photograph of the top and bottom of the fabricated force sensor. The chip measures 4 mm by 3 mm.

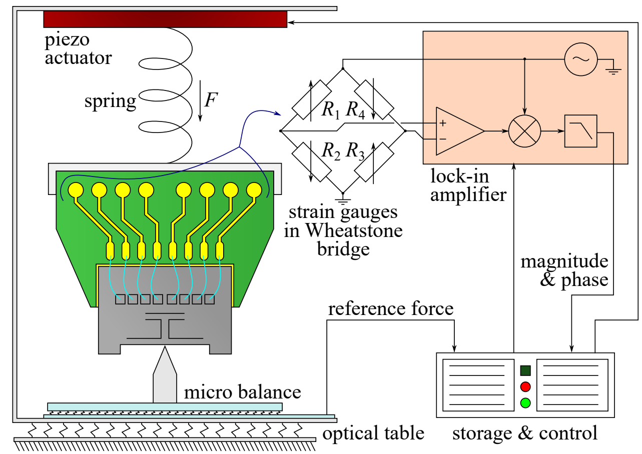

Figure 5: Schematic diagram of the measurement setup for the static characterization. A piezo actuator and spring apply force on the device under test and a microbalance reference. Lock-in amplification is used to detect the bridge voltage of the strain gauges.

measure the bridge voltage. For reference, a microbalance (Mettler Toledo® AT200) has been used.

The acquired results with a model fit based on equation (8) are shown in Figure 6. The total measurement time was approximately 3.5 hours. The results show that the sensor has a range of 13 mN with high linearity ($R^2 > 0.9999$), a sensitivity of 1.46 N^{-1} and a standard deviation-based accuracy of 100 µN.

The frequency behavior of the sensor has been measured by laser Doppler vibrometry (Polytec® MSA-600) with external piezo actuation and is compared to the calculated resonance frequency and FEM simulations. Figure 7 shows that the resonance frequency for the first vibrational mode is at 75 kHz which gives a measure for the bandwidth. Figure 8 shows the first three measured vibrational modes. The measured resonance frequency is lower than expected, which could be caused by non-ideal etching profiles.

A comparison of the measurement results with calculations and simulations is shown in Table 2.

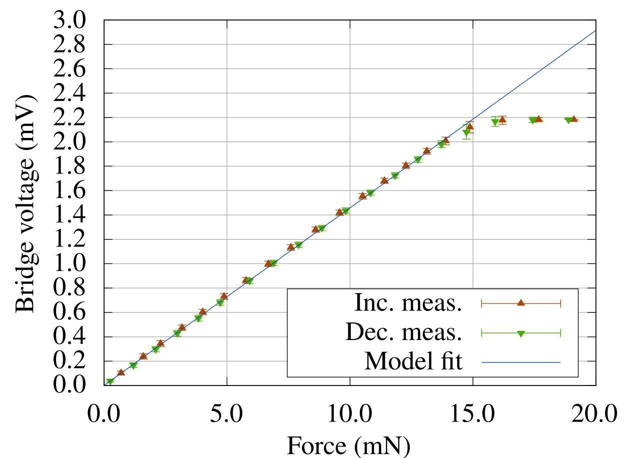

Figure 6: Measured bridge voltages (offset corrected) for applied forces with standard deviation (errorbars), in increasing (▲) and decreasing (▼) order compared with model fit (–).

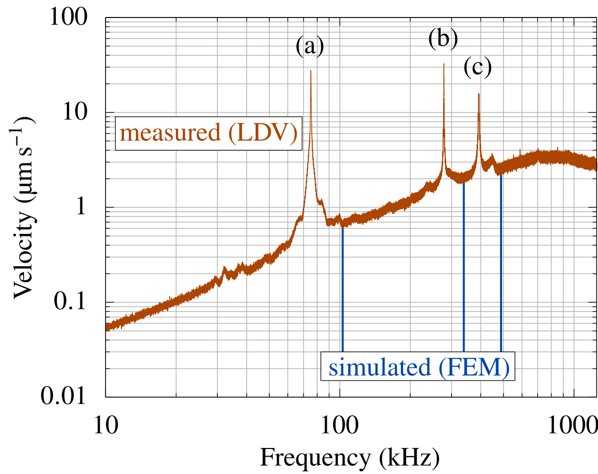

Figure 7: Frequency spectrum of averaged velocity magnitudes for all points on the sense beam measured using laser Doppler vibrometry and compared with FEM simulations.

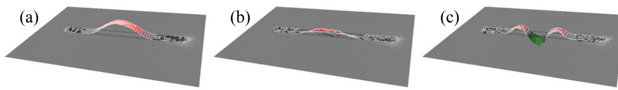

Figure 8: First three measured vibrational modes corresponding to the magnitude peaks (a, b and c) in Figure 7.

Table 2: Comparison of calculated, simulated, and measured values for the spring constant (k), sensitivity (V_b/V_sF^{-1}), and resonance frequency (f_0).

	Calculated	Simulated	Measured
k	$18\,\mathrm{kN\,m^{-1}}$	$18.7\,\mathrm{kN\,m^{-1}}$	N/A
V_b/V_sF^{-1}	$1.39\,\mathrm{N^{-1}}$	$1.34\,\mathrm{N^{-1}}$	$1.46\,\mathrm{N^{-1}}$
f_0	110 kHz	103 kHz	75 kHz

CONCLUSION

A force sensor with a a range of 13 mN, a sensitivity of $1.46\,\mathrm{N^{-1}}$, and a bandwidth of 75 kHz has been designed, fabricated, and characterized. Miniaturization and mechanical amplification are essential to achieve these contradicting specifications for the bandwidth and sensitivity. This novel combination allows this sensor to serve in new fields of low force sensing, e.g., the measurement of microscale and microsecond impact behavior of liquids.

The mechanical amplification (and thus sensitivity) can be increased by improving the transmission from sense beam to strain gauge beam (i.e., by cantilever bending). Future work will also focus the development of multiple sensors with different specifications, integration of multiple sensing beams for tactile sensing, and measuring the impact of microdroplets.

ACKNOWLEDGEMENTS

The authors gratefully acknowledge support by Sectorplan Bèta and Techniek, Europees Fonds voor Regionale Ontwikkeling through the METEORIET project, and the European Research Council (ERC) under the European Union Horizon 2020 Research and Innovation Programme (grant agreement no. 851630).

REFERENCES

[1] M. Elhadi Ibrahim *et al.*, "Water droplet erosion of wind turbine blades: Mechanics, testing, modeling and future perspectives," *Materials*, vol. 13, no. 1, p. 157, 2020.

[2] H. Wijshoff, "Drop dynamics in the inkjet printing process," *Current Opinion in Colloid & Interface Science*, vol. 36, pp. 20–27, 2018.

[3] S. Mitragotri, "Current status and future prospects of needle-free liquid jet injectors," *Nature reviews Drug discovery*, vol. 5, no. 7, pp. 543–548, 2006.

[4] A. Mohizin *et al.*, "Impact of the mechanical properties of penetrated media on the injection characteristics of needle-free jet injection," *Experimental Thermal and Fluid Science*, vol. 126, p. 110396, 2021.

[5] J. C. Stachowiak *et al.*, "Piezoelectric control of needle-free transdermal drug delivery," *Journal of Controlled Release*, vol. 124, no. 1-2, pp. 88–97, 2007.

[6] A. M. Römgens *et al.*, "Penetration and delivery characteristics of repetitive microjet injection into the skin," *Journal of Controlled Release*, vol. 234, pp. 98–103, 2016.

[7] L. Oyarte Gálvez *et al.*, "Microfluidics control the ballistic energy of thermocavitation liquid jets for needle-free injections," *Journal of Applied Physics*, vol. 127, no. 10, p. 104901, 2020.

[8] M. R. Prausnitz *et al.*, "Transdermal drug delivery," *Nature Biotechnology*, vol. 26, no. 11, pp. 1261–1268, 2008.

[9] Y. Zhang *et al.*, "Advances in transdermal insulin delivery," *Advanced Drug Delivery Reviews*, vol. 139, pp. 51–70, 2019.

[10] K. Cu *et al.*, "Delivery strategies for skin: Comparison of nanoliter jets, needles and topical solutions," *Annals of Biomedical Engineering*, vol. 48, no. 7, pp. 2028–2039, 2020.

[11] M. Maroufi *et al.*, "An adjustable-stiffness mems force sensor: Design, characterization, and control," *Mechatronics*, vol. 56, pp. 198–210, 2018.

[12] Y. Sun *et al.*, "Drosophila flight force measurements using a mems micro force sensor," in *The 26th Annual International Conference of the IEEE Engineering in Medicine and Biology Society*, vol. 1. IEEE, 2004, pp. 2014–2017.

[13] F. Beyeler *et al.*, "A six-axis mems force–torque sensor with micro-newton and nano-newtonmeter resolution," *Journal of Microelectromechanical Systems*, vol. 18, no. 2, pp. 433–441, 2009.

[14] W. C. Young *et al.*, *Roark's formulas for stress and strain*. McGraw-hill New York, 2002, vol. 7.

[15] D. Schubert *et al.*, "Piezoresistive properties of polycrystalline and crystalline silicon films," *Sensors and Actuators*, vol. 11, no. 2, pp. 145–155, 1987.

[16] M.-H. Bao, *Handbook of Sensors and Actuators*. Elsevier Science B.V., 2000, vol. 8.

[17] D. Alveringh *et al.*, "A large range multi-axis capacitive force/torque sensor realized in a single soi wafer," in *2014 IEEE 27th International Conference on Micro Electro Mechanical Systems (MEMS)*. IEEE, 2014, pp. 680–683.

CONTACT

Dennis Alveringh – d.alveringh@utwente.nl